A study of secondary instabilities in postbuckling composite aerostructures

B. G. Falzon
Department of Aeronautics
Imperial College London, UK

M. Cerini
Adams Kara Taylor
London, UK.

ABSTRACT

A number of experimental studies have shown that postbuckling stiffened composite panels, loaded in uniaxial compression, may undergo secondary instabilities, characterised by an abrupt change in the buckled mode-shape of the skin between the supporting stiffeners. In this study high-speed digital speckle photogrammetry is used to gain further insight into an I-stiffened panel's response during this transient phase. This energy-dissipating phenomenon will be shown to be able to cause catastrophic structural failure in vulnerable structures. It is therefore imperative that an accurate and reliable methodology is available to predict this phenomenon. The shortcomings of current non-linear implicit solution schemes, found in most commercially-available finite element codes, are discussed. A robust and efficient strategy, which utilises an automated quasi-static/pseudo-transient hybrid scheme, is presented in this paper and validated using a number of experimental tests. This approach is shown to be able to predict mode-jumping with good accuracy.

NOMENCLATURE

a_i	quadratic coefficients (i = 1,2,3)
d	diagonal entry in **D**
$\mathbf{f}(\mathbf{u})$	vector of internal forces as a function of displacements
$\mathbf{f}_{ext}$	fixed external load vector
$\mathbf{g}$	vector of residual forces
$\boldsymbol{l}_i$	column of $(L^T)^{-1}$ corresponding to $(d_{ii})_{min}$
t	time at the start of the step
$\mathbf{u}$	displacements vector
$\dot{\mathbf{u}}$	velocity vector
$\ddot{\mathbf{u}}$	acceleration vector
$\mathbf{C}$	damping matrix
$\mathbf{D}$	diagonal matrix of factored stiffness matrix
$\mathbf{K}_t$	tangential stiffness matrix
$\overline{\mathbf{K}}_t$	previous estimate of tangential stiffness matrix
$\mathbf{K}_{tA}$	tangential stiffness matrix at some point A
$\mathbf{K}_{tB}$	tangential stiffness matrix at some point B
$\mathbf{K}_{tC}$	tangential stiffness matrix at some point C
$\mathbf{L}$	lower unit triangular matrix
$\mathbf{M}$	mass matrix
α	interpolation parameter
γ_A	smallest eigenvalue of $\mathbf{K}_{tA}$
γ_B	smallest eigenvalue of $\mathbf{K}_{tB}$
$\delta\alpha$	small fraction of α
$\delta\lambda$	iterative change in the applied load
λ	load multiplier
τ	time variable
μ	scaling parameter
$\boldsymbol{\varphi}$	eigenvector
ψ	scaling parameter
ω_{max}	maximum resonant frequency
ω_{min}	minimum resonant frequency
Δl	arc-length constraint
Δt	time step
$\Delta\mathbf{u}$	incremental change in displacement
$\Delta\lambda$	incremental change in load multiplier

Paper No. 3171. This is an invited paper published to celebrate the 100th anniversary of Imperial College, London.

https://doi.org/10.1017/S0001924000004899 Published online by Cambridge University Press

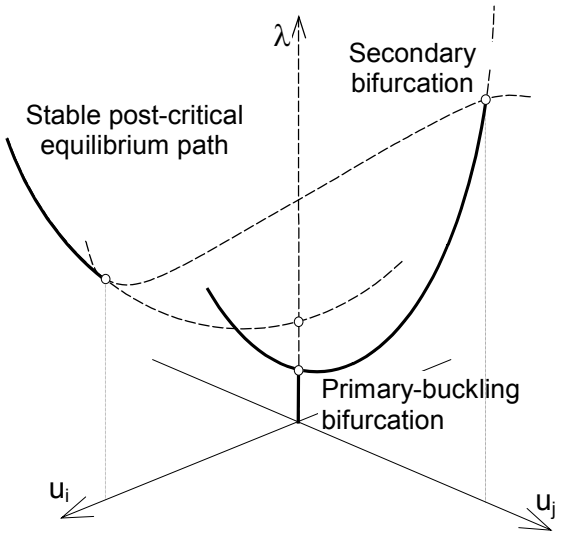


Figure 1. Equilibrium paths showing primary and secondary instabilities (solid lines: stable states; dashed lines: unstable states).

Subscripts

A, *B*, *C*, *D*	points along an equilibrium path
ext	external
i	position of column , ***l***, in **L**
ii	position of diagonal term, *d*, in **D**
max	maximum
min	minimum
t	tangential

1.0 INTRODUCTION

A considerable number of experimental programmes within the department of Aeronautics at Imperial College London[1-6] and elsewhere[7-10] have demonstrated the ability of composite panels to support compressive loads beyond initial skin-buckling. The prospect of allowing certain parts of an aerostructure to operate in a postbuckled state, between the design limit and ultimate loads, or indeed even below the design limit load, offers the possibility of developing very lightweight aerostuctures. In a recent European Union document outlining the future of aeronautics[11], the reduction in environmental impact featured prominently. One target is a 50% reduction in fuel consumption and an 80% reduction in nitrous oxide emissions by 2020. A significantly lighter structure will contribute towards meeting these goals.

Postbuckled stiffened composite structures, despite the promise of contributing to achieving this goal, give rise to high through-thickness stresses at the skin-stiffener interfaces which are only resisted by the strength of the matrix or the adhesive. This has lead to a reluctance, by industry, to exploit their reserve strength. While the possibility of using mechanical fasteners exists, these create considerable problems of their own. The added stress concentrations which may arise around a fastener hole due to slight dimensional inaccuracies are not easily diffused in a composite component, as they are in metallic structures. Hence the future development of these structures will continue to exploit co-curing, co-bonding, secondary-bonding or resin-infusion processes which minimise the need for fasteners.

The postbuckling behaviour of stiffened composite structures is further complicated by the observed sudden change in buckling mode-shape. This phenomenon is a secondary instability and is commonly referred to as a mode-jump or a mode-switch. Primary skin-buckling is characterised by a stable bifurcation point which defines the intersection of the primary and a secondary stable equilibrium path. For secondary instabilities in plate structures, the bifurcation point is the intersection of the current stable equilibrium path with at least one unstable equilibrium path, which eventually leads to a stable post-critical branch. This concept is shown schematically in Fig. 1, where u_i and u_j are generalised co-ordinates representing a deformation mode and λ is a load parameter.

At high loading, this sudden energy-dissipating phenomenon may release enough energy to cause damage on first occurrence and previous experimental tests conducted by Falzon *et al*[2] and Romeo and Frulla[12] have yielded indirect evidence of failure of some test panels by mode-jumping. This paper presents more substantial evidence of this occurrence in testing a hat-stiffened panel.

It is therefore imperative that the future design of postbuckling structures will utilise robust computational tools capable of predicting this abrupt behaviour. Numerical modelling of postbuckling structures has conventionally been performed using implicit continuation methods. It is well established that standard non-linear solution schemes such as the Newton-Raphson methods fail when they encounter such behaviour. While other implicit continuation schemes, such as the arc-length method[13-15], have been developed to handle highly non-linear behaviour, they may still run into difficulty in the presence of mode-jumping. One possibility of analysing these structures is to use a full dynamic analysis but this is computationally expensive. A more effective strategy for capturing mode-jumping is to use a combined static-dynamic analysis and this was demonstrated by Riks *et al*[16] where the switching from one solution procedure to the other was performed interactively using restarting schemes available in most finite element packages and utilising standard implicit or explicit dynamic schemes.

In this paper an automated quasi-static/pseudo-transient procedure is presented which is capable of accurately capturing secondary instabilities. The static part of the solution process uses an implicit continuation scheme. A modified explicit dynamic routine, which is more computationally efficient than standard implicit or explicit dynamic schemes, is used for the transient phase. Strategies for determining the location and type of critical points along an equilibrium path, and for switching to a secondary path, are presented.

Table 1
Material properties for carbon-fibre unidirectional prepreg T300/914C

Property (RT/Dry)	Value
Longitudinal tensile Young's modulus, E_{1t}	135GPa
Longitudinal compressive Young's modulus, E_{1c}	120GPa
Transverse tensile Young's modulus, E_{2t}	9·0GPa
Transverse compressive Young's modulus, E_{2c}	9·0GPa
In-plane shear modulus, ν_{12}	0·28
Nominal ply thickness	0·125mm

2.0 EXPERIMENTAL PROGRAMME

2.1 I-stiffened panel

Two I-stiffened panels, designated I-P1 and I-P2, were manufactured from T300/914C unidirectional pre-impregnated composite (material properties are shown in Table 1) with a nominal skin-thickness of 2·0mm. Four equally-spaced stiffeners were secondary-bonded onto the skin using FM300 adhesive film. Panel I-P1 was tested in a

https://doi.org/10.1017/S0001924000004899 Published online by Cambridge University Press

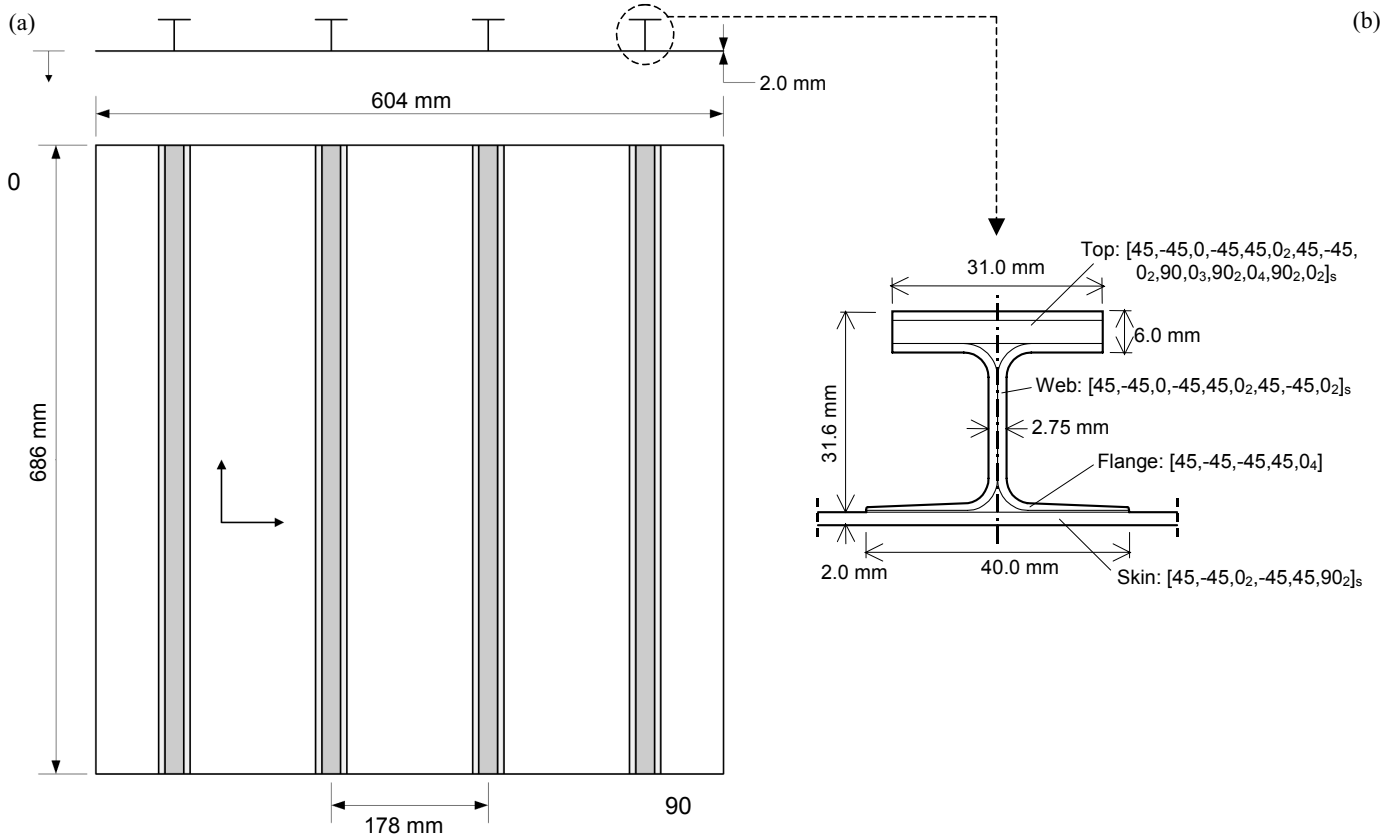


Figure 2. I-stiffened panel, I-P2; (a) major dimensions and (b) details of the stiffener cross section.

custom-built 250 ton hyperstiff testing machine[17] in the Department of Aeronautics at Imperial College London while I-P2 was tested at the DLR Institute of Structural Mechanics in Braunschweig, Germany, using a 1 MN servo-hydraulic testing facility and a newly developed high-speed non-contact full-field measuring system to directly observe the mode-jumping. The effective test sections were 790mm × 604mm for I-P1 and 686mm × 604mm for I-P2. A schematic showing the major dimensions of IP-2 and the lay-up details of the stiffener are given in Fig. 2.

In a numerical study conducted by Bushnell *et al*[18] it was postulated that the possibility of damage during a mode-jump depended on the frequency of occurrence in service, the number and amplitude of stress oscillations resulting from the jump, whether these oscillations involved stress reversal and the energy released in the process. To gain further insight into this phenomenon, the ARAMIS[19] high-speed non-contact full-field measuring system was used. The ARAMIS set-up requires that the surface being measured is initially painted white and then sprayed with a black speckle pattern to create a distribution of greyscale values. The basic system uses two cameras and processing software to track changes in the relative position of the speckles. Displacement and strain values for a structure under loading are obtained using photogrammetry principles. The high-speed set-up at DLR uses four ARAMIS systems each with a pair of high-speed cameras able to sample at a quoted rate of 1kHz. In practice, the maximum capture rate that was achieved was 833Hz. The recording of images between these four systems was staggered resulting in a maximum sampling speed of 3·33kHz. Figure 3 shows the panel mounted in the servo-hydraulic testing machine in the foreground with the eight cameras mounted in the background.

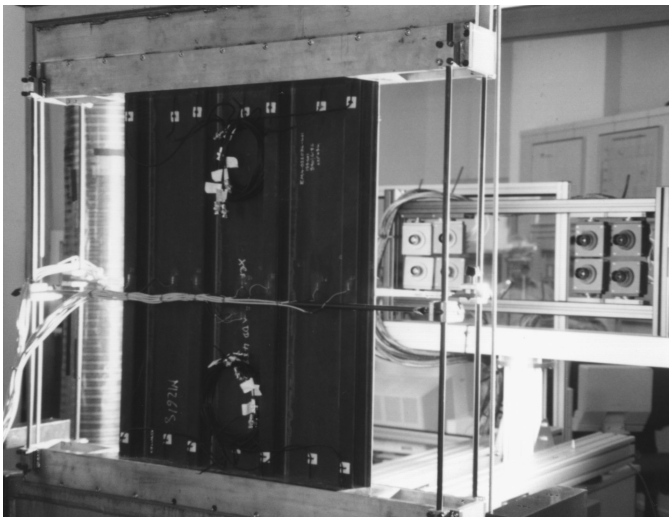
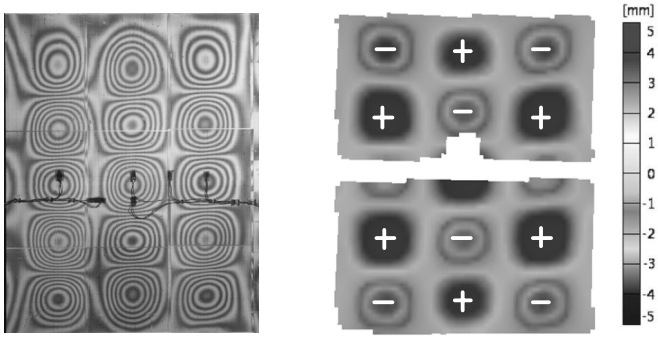


Figure 3. Panel mounted in testing machine (foreground) with the eight DSP cameras shown in the background.

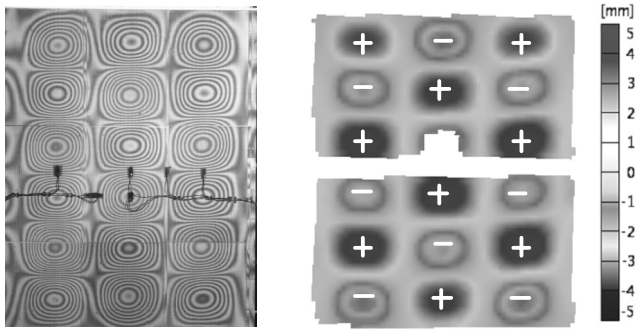
Both panels were loaded in uniaxial compression; IP-1 until failure while the test on IP-2 was terminated at a loading of 387kN. The aspect ratio of the skin-bays in IP-1 was 4·43 while for IP-2 the aspect ratio was 3·85. Each panel displayed a five half-waves initial skin-buckling pattern. Figure 4(a) shows the Moiré fringe pattern obtained from the test on IP-1 and Fig. 4(b) shows a contour plot of panel IP-2 obtained from the DSP system.

https://doi.org/10.1017/S0001924000004899 Published online by Cambridge University Press



(a) (b)

Figure 4. (a) Moiré fringe pattern of IP-1 at a loading of 190 kN, (b) Digital speckle photogrammetry contours of IP-2 at a loading of 349 kN. The (+) and (-) signs on each half wave indicate whether the displacement is into the page (+) or out of the page (-).



(a) (b)

Figure 5. (a) Moiré fringe pattern of IP-1 at a loading of 245 kN (b) Digital speckle photogrammetry contours of IP-2 at a loading of 387 kN. The (+) and (-) signs on each half wave indicate whether the displacement is into the page (+) or out of the page (-).

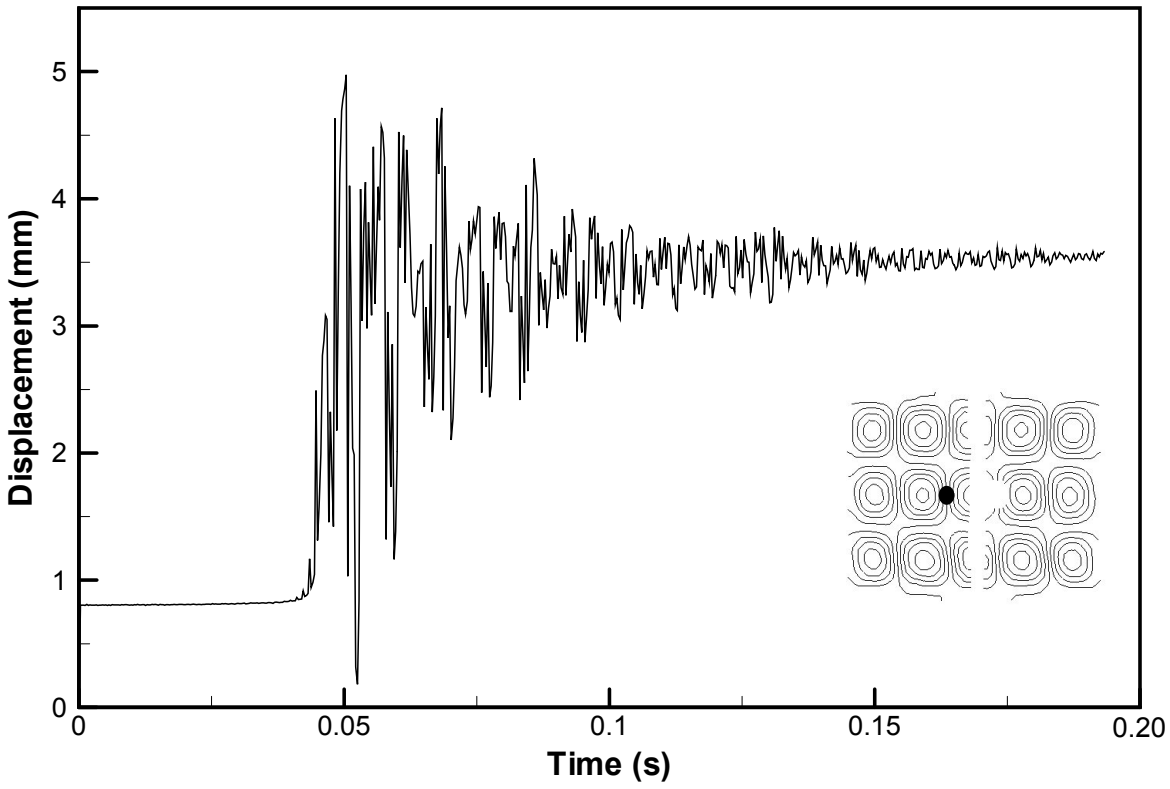


Figure 6. Out-of-plane displacement close to an initial node-line during the mode-jump.

Strain gauge wiring mounted across the panel's centre masked the speckle in that region resulting in the missing contour sections. The initial skin buckling load of Panel IP-1 was recorded at 120kN and for IP-2 at 125kN. This difference is consistent with the variation in aspect ratio of the respective skin bays. Both panels displayed a sudden secondary instability to a six half-waves pattern but this occurred at different loading in each panel: at 244kN for IP-1 and 366kN for IP-2, shown in Fig. 5. It is evident that while the different aspect ratios had a small effect on the initial buckling load, the influence on the secondary instability was more pronounced.

A major motivation for using the high-speed DSP system was to gain further insight into the transient phenomenon associated with secondary instabilities. Figure 6 shows the out-of-plane displacement recorded in the vicinity of a node-line. The mode-jump

https://doi.org/10.1017/S0001924000004899 Published online by Cambridge University Press

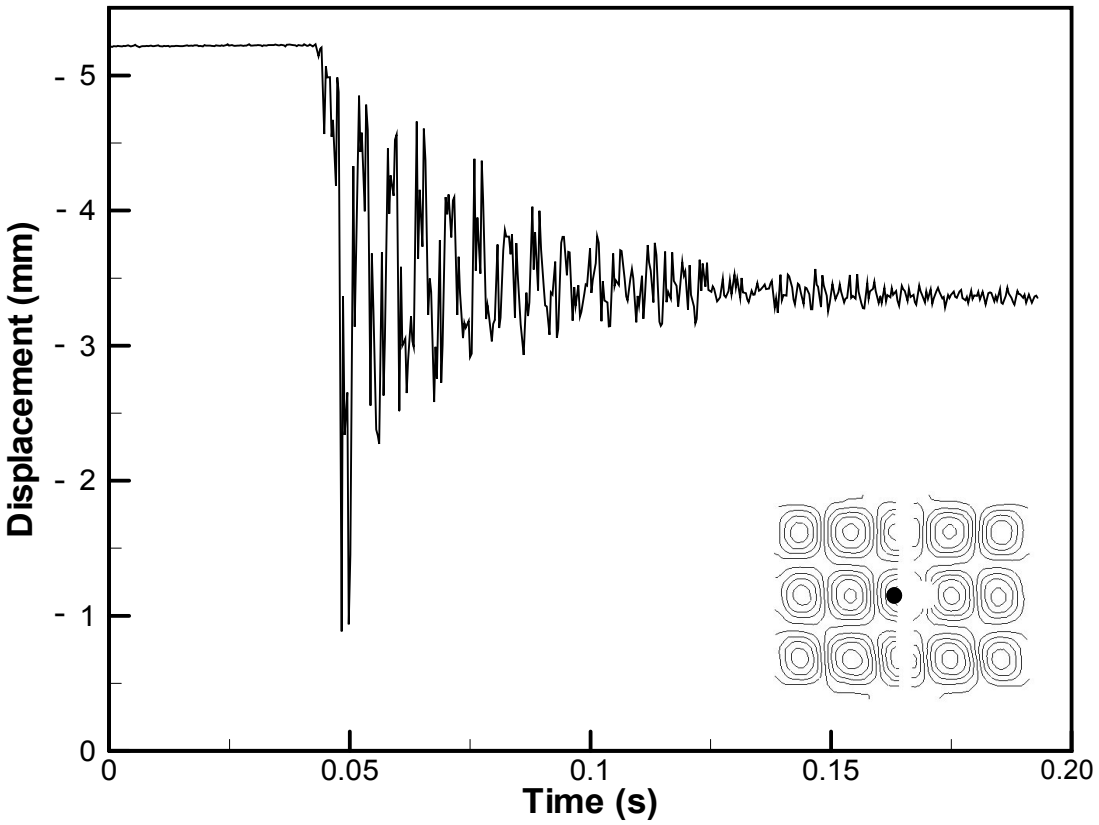


Figure 7. Out-of-plane displacement close to an initial crest during the mode-jump.

is characterised by high-frequency oscillations which are damped over a period of approximately 106 milliseconds. There is a jump in out-of-plane displacements from 0·8mm to 3·55mm but with peak displacements reaching 4·93mm. Figure 7 shows the out-of-plane displacement in the vicinity of an initial crest (anti-node-line) during the mode-jump. The high-frequency oscillations are again observed during the transient phase and it is noted that at this location there is a sudden drop in displacement arising from the creation of an extra half-wave as the mode-shape changes from five to six half-waves and where this location now corresponds to a region closer to a node-line. In Fig. 8, a strain plot is shown for this transient phase. An increased level of noise is observed in these results. This is attributed to additional computations involving the formation of a deformation gradient tensor which relates the position of the speckle in the undeformed state to their position in the deformed state. Short-term strain peaks, considerably higher than the quasi-static value obtained after the mode-jump, were recorded. The stress reversal predicted by the simulation presented by Bushnell *et al*[18] was not observed in this test.

2.2 Hat-stiffened panel

A hat-stiffened panel with skin-bays of identical dimensions and lay-up to I-P1 was manufactured. The stiffeners were designed to have a similar proportion of 0°, 90° and ±45° plies to that of the I-stiffeners resulting in a second moment of area of the cross-section which was approximately 17% higher[20]. The stiffeners were secondary bonded onto the skin and the manufactured panel, before trimming, is shown in Fig. 9(a). Figure 9(b) shows the panel mounted in the 250T compression testing machine.

This panel was loaded in compression and failed prematurely at a loading of 380kN without a mode-jump being detected. Extensive stiffener debonding was observed. This panel was expected to sustain a load at least equal to that sustained by I-P1 (well over 500kN) before final failure.

3.0 NUMERICAL ANALYSIS

Bifurcation along an equilibrium path, representing the intersection with a secondary path, presents particular difficulties in standard non-linear finite element solution schemes. A common strategy is to remove the presence of bifurcations by adding geometric imperfections to the structure where the response is represented by a single equilibrium path, albeit one which may display the presence of limit points. These are points along an equilibrium path where the stiffness is reduced to zero. A number of solution techniques have been developed over the years to traverse these limit points and the interested reader is referred to the monograph by Falzon and Hitchings[21] which discusses a number of these strategies.

https://doi.org/10.1017/S0001924000004899 Published online by Cambridge University Press

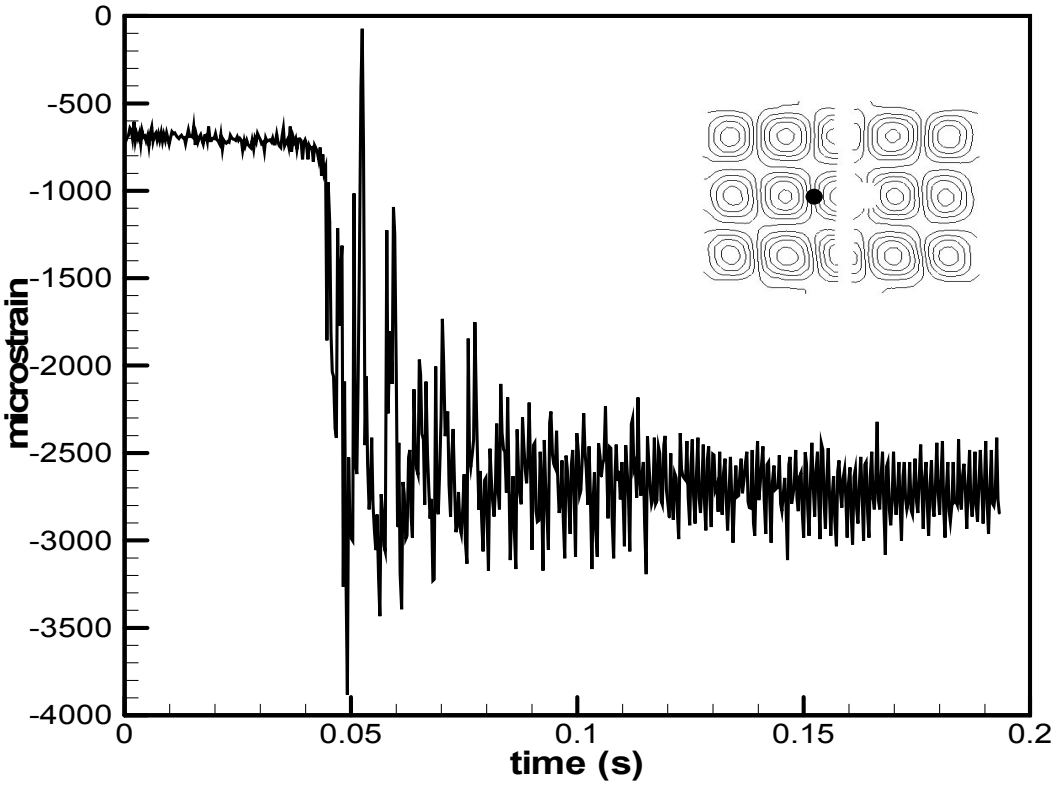


Figure 8. Longitudinal direct strain at an initial node-line during the mode-jump.

3.1 The arc-length method

The arc-length method[13-15] has emerged as one technique which is being widely adopted in a number of non-linear finite element packages. This method is based on augmenting the system of non-linear equilibrium equations:

$$\boldsymbol{g}(\boldsymbol{u},\lambda) = \boldsymbol{f}(\boldsymbol{u}) - \lambda \boldsymbol{f}_{ext} = 0 \qquad \ldots (1)$$

with an incremental constraint which is a function of both the incremental displacements and the load increment:

$$\Delta \boldsymbol{u}^T \Delta \boldsymbol{u} + \Delta\lambda^2 \psi^2 \boldsymbol{f}_{ext}^T \boldsymbol{f}_{ext} = \Delta l^2 \qquad \ldots (2)$$

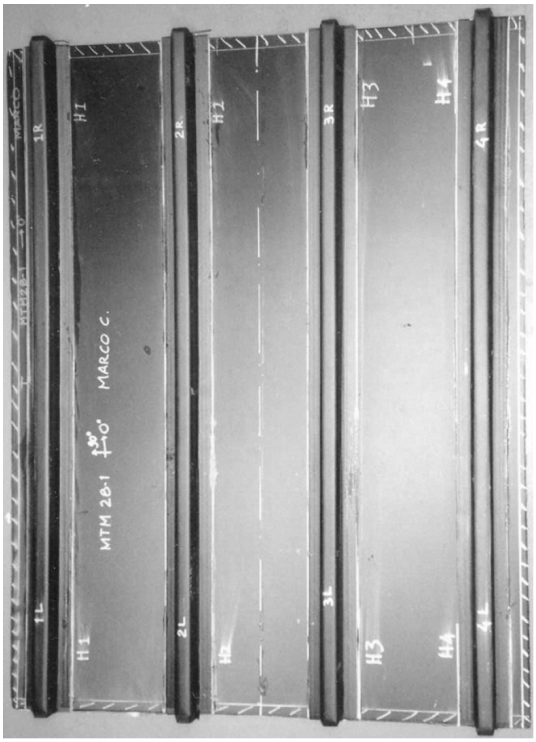
A graphical representation of this scheme is given in Fig. 10 where, for clarity, the equilibrium curve is plotted as a function of two variables; a displacement, u, representing the displacement vector, **u**, and an external load, f_{ext}, representing the external load vector, $\mathbf{f}_{ext}$. Riks' formulation[14] iterates along a hyperplane, orthogonal to the tangent, produced to length Δl, from a previously converged point along the equilibrium path. Crisfield's method[15] iterates along a hypersphere, where the arc-length constraint is also employed for corrector iterations, and is less likely to fail in the vicinity of sharp limit points. Crisfield has further shown that the loading terms have little influence on the solution process and advocated setting $\psi = 0$. The iterations within each increment are usually performed using a modified Newton-Raphson scheme where the tangential stiffness matrix is held fixed within each increment.

Solving Equation (1) and Equation (2) simultaneously is not readily amenable to finite element analysis since the augmented stiffness matrix will not be symmetric or banded. Using an approach suggested by Batoz and Dhatt[22] this system of equations reduces to a quadratic in which $\delta\lambda$ represents an iterative change in the applied load:

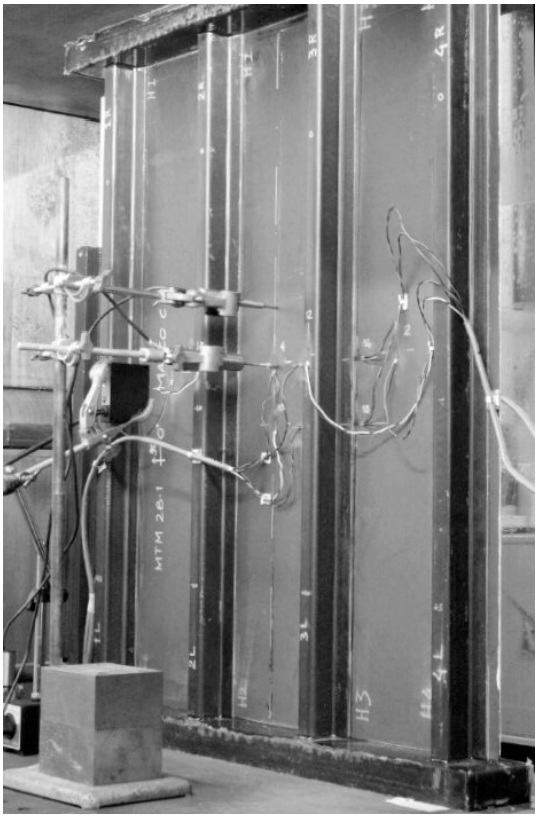
$$a_1 \delta\lambda^2 + a_2 \delta\lambda + a_3 = 0 \qquad \ldots (3)$$

The expressions for the quadratic coefficients a_1, a_2 and a_3 are given by Crisfield[23] This implies two possible solutions for the load increment and the correct choice of $\delta\lambda$, at the predictor stage, is central to this method's effectiveness. One possibility is to match the sign of $\delta\lambda$ with the determinant of the stiffness matrix. In practice this is achieved by looking at terms of the diagonal matrix **D** of the factored tangential stiffness matrix, $\mathbf{K}_t = \mathbf{LDL}^T$, where **L** is a lower unit triangular matrix. If all terms on the diagonal are positive this implies the stiffness matrix is positive definite and hence a positive sign for the load increment is chosen. If a negative diagonal is encountered this is equivalent to detecting a negative eigenvalue and implies that a limit point has been passed. Hence a negative load increment is applied. The arc length method is able to trace both the stable and unstable sections of an equilibrium curve although it is still liable to fail in the vicinity of 'sharp' limit points.

https://doi.org/10.1017/S0001924000004899 Published online by Cambridge University Press



(a)



(b)

Figure 9. (a) Secondary bonded hat-stiffened panel; (b) panel mounted in 250T compression testing machine.

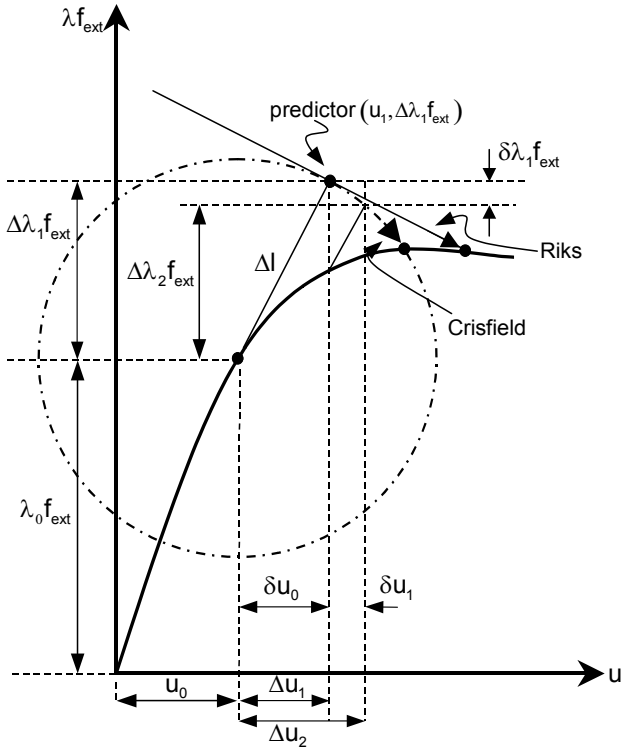


Figure 10. Arc-length constraint schemes proposed by Riks and Crisfield.

If the arc-length routine is used in the presence of a bifurcation point (which is also detected by a change in the sign of a term in **D**) the solution will tend to oscillate. This comes about because if such a point is passed, then a negative entry in **D** will invoke a negative load increment. This may well bring the solution below the critical load which would imply that $\mathbf{K}_t$ is positive-definite and hence a positive load increment is used which could, in turn, result in the solution being past the bifurcation load and therefore as this process is repeated, oscillation occurs about the bifurcation point.

3.2 Dynamic methods

The problem of mode-jumping could be solved using dynamic analysis. Indeed this approach has been adopted in a number of numerical studies[9-10,24]. The dynamic equations of motion are to be solved at some time $\tau = t + \Delta t$, where Δt is the time-step (or time increment) and t is the time at the start of the step. Two solution methods are available for solving these equation; an implicit solution where the 'exact' equations are solved for $\tau = t + \Delta t$, or an explicit solution where the equations are solved approximately.

For an implicit solution scheme the equations of motion are solved at $\tau = t + \Delta t$:

$$ {}^{t+\Delta t}\mathbf{M}\,{}^{t+\Delta t}\ddot{\mathbf{u}} + {}^{t+\Delta t}\mathbf{C}\,{}^{t+\Delta t}\dot{\mathbf{u}} + {}^{t+\Delta t}\mathbf{K}_t\,{}^{t+\Delta t}\mathbf{u} = {}^{t+\Delta t}\lambda \boldsymbol{f}_{ext} \qquad \ldots (4) $$

This system of equations must be solved iteratively using identical iterative solution techniques employed in static analysis.

https://doi.org/10.1017/S0001924000004899 Published online by Cambridge University Press

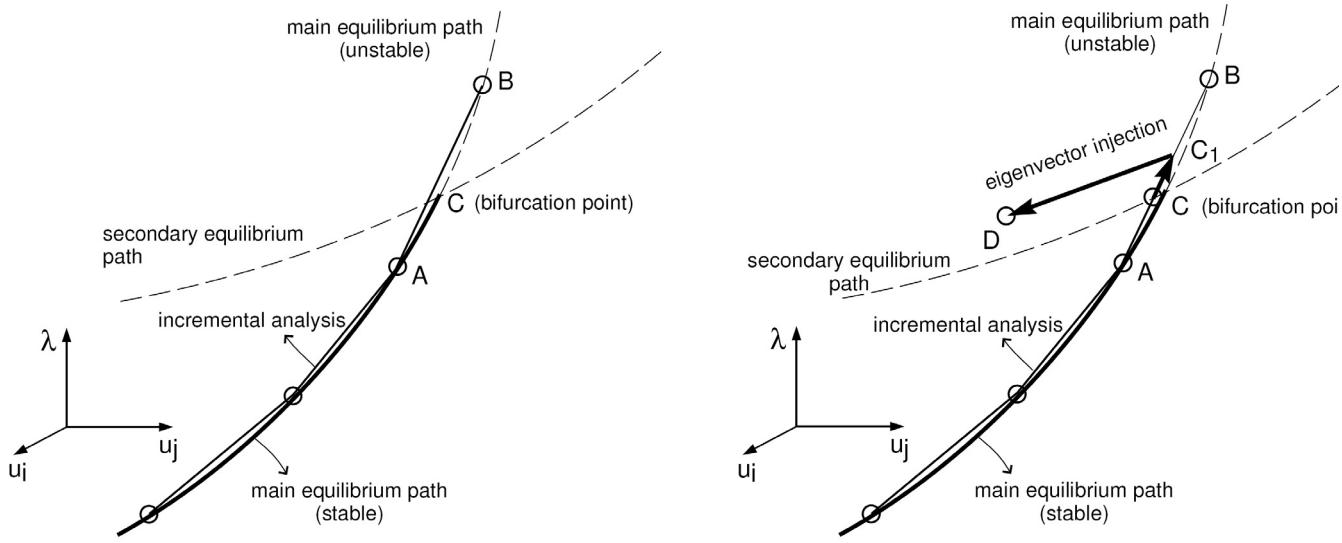


Figure 11. Intersecting equilibrium paths showing the location of a critical point *C* and point *D* which denotes the initial conditions for the pseudo-transient phase.

For the explicit solution scheme, the initial condition, for a sufficiently small time step, may be approximated as:

$$\left(\mathbf{M}\,{}^{t+\Delta t}\ddot{\mathbf{u}} + {}^{t}\mathbf{C}\,{}^{t}\dot{\mathbf{u}} + {}^{t}\mathbf{K}_{t}\,{}^{t}\mathbf{u}\right) = {}^{t+\Delta t}\lambda \boldsymbol{f}_{ext} \qquad \ldots (5)$$

Where the superscript on **M** has been dropped since it is assumed that the mass remains constant. This method is very stable for highly non-linear behaviour but it is conditionally stable, i.e., the time-step has to be less than a certain critical value which is of the order of the inverse of the maximum resonant frequency of the finite element model.

The solution is approximate but computationally efficient, especially if the mass matrix is assumed to be diagonal. Since the time step, Δt, is small, many steps are required but each step can be computed quickly. The efficiency is made even greater by recognising that the product ${}^{t}\mathbf{K}_{t}{}^{t}\mathbf{u}$ can be carried out on an element-by-element basis and the global stiffness matrix need not be formed. While the time-step size is controlled by the highest resonant frequency, ω_{max}, the duration of the calculation to achieve a static solution, as would be required beyond the mode-jump, is governed by the lowest resonant frequency, ω_{min}. This implies that the number of cycles required to recover a static solution is proportional to the ratio of the highest to lowest resonant frequencies. An artificial mass matrix is often used to reduce the span of the resonant frequencies of the structure. However, the use of a diagonal matrix, for computational efficiency, limits what can be done. Selectively scaling the mass of specific elements allows some control over reducing ω_{max}. Another means of speeding up the solution time is to increase the load rate but this needs to be introduced with caution, to ensure that inertial effects are not introduced during the static phase of the actual loading history.

3.3 An automated quasi-static/pseudo-transient method

It has been argued that the computational time required to recover a static solution using explicit dynamic analysis is governed by the use of a diagonal mass matrix and the ratio $\omega_{max}/\omega_{min}$. This ratio may be reduced to unity if we replace **M** and **C** by $\mathbf{K}_t$:

$$\bar{\mathbf{K}}_{t}\,{}^{t+\Delta t}\ddot{\mathbf{u}} + \mathbf{K}_{t}\,{}^{t}\dot{\mathbf{u}} + {}^{t}\mathbf{K}_{t}\,{}^{t}\mathbf{u} = {}^{t+\Delta t}\lambda \boldsymbol{f}_{ext} \qquad \ldots (6)$$

This scheme was implemented by the authors[6] where it is noted that a bar is added over the stiffness matrix replacing the mass matrix to indicate that this matrix was only updated periodically to reduce computational effort. One small drawback here is that we no longer have a diagonal form of the matrix to be inverted as the emphasis is shifted to reducing $\omega_{max}/\omega_{min}$. In practice, the solution scheme was further improved by removing second order terms altogether so that a transient scheme was used:

$$\bar{\mathbf{K}}_{t}\,{}^{t+\Delta t}\dot{\mathbf{u}} + {}^{t}\mathbf{K}_{t}\,{}^{t}\mathbf{u} = {}^{t+\Delta t}\lambda \boldsymbol{f}_{ext} \qquad \ldots (7)$$

By assuming a linear variation in velocity over the time-step, Δt, the following equations were solved incrementally:

$$\begin{aligned} {}^{t+\Delta t}\dot{\mathbf{u}} &= \bar{\mathbf{K}}_{t}^{-1}\left({}^{t+\Delta t}\lambda \boldsymbol{f}_{ext} - {}^{t}\mathbf{K}_{t}\,{}^{t}\mathbf{u}\right) \\ {}^{t+\Delta t}\boldsymbol{u} &= \left(1 + \frac{\Delta t}{2}\right){}^{t}\dot{\boldsymbol{u}} + \frac{\Delta t}{2}\,{}^{t+\Delta t}\dot{\boldsymbol{u}} \end{aligned} \qquad \ldots (8)$$

This method also allows for a large time-step in comparison to a standard explicit analysis. It can easily be shown that if $\mathbf{K}_t$ is used instead of $\bar{\mathbf{K}}_t$ (at the expense of increased computational time when inverting this matrix at every increment) the condition for stability is that $\Delta t \leq 1$. In practice, Δt was limited to 0·4 in the analysis presented later in this paper. The ratio of the norms of the out-of-balance force to the applied load $\left\|{}^{t+\Delta t}\lambda \boldsymbol{f}_{ext} - {}^{t}\boldsymbol{K}_{t}\,{}^{t}\boldsymbol{u}\right\| / \left\|{}^{t+\Delta t}\lambda \boldsymbol{f}_{ext}\right\|$ was used to check convergence and the change of this was used to adjust Δt, to speed up convergence if the change was small and to reform the current tangent stiffness matrix estimate, $\bar{\mathbf{K}}_t$, if the out-of-balance force was increasing significantly.

This pseudo-transient method may be used on its own to solve problems involving mode-jumping[6] but the experimental observations discussed earlier show that for the most part of the loading history, the panel only displays 'mild' non-linear behaviour which is easily captured using standard methods of non-linear numerical analysis. It is only when a critical point is reached (whether a bifurcation or a limit point) that a more robust scheme needs to be employed. The strategy adopted for this present study was to use either a Newton-Raphson or arc-length algorithm to initiate the analysis and to continue with this scheme as long as the tangential stiffness matrix remained positive definite. This is represented by the

https://doi.org/10.1017/S0001924000004899 Published online by Cambridge University Press

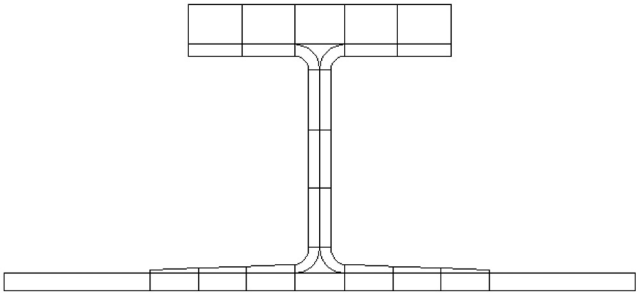


Figure 12. Finite element discretisation of stiffener section.

bold curve in Fig 11(a) where point A along the equilibrium curve represents a stable configuration. For simplicity these curves have been plotted as a function of the load parameter, λ, and two generalized displacements u_i and u_j. When point C is passed, a negative pivot (diagonal term in **D**) is detected and a bracketing procedure[25] is invoked to reduce the distance between points A and B to within a pre-determined arc-length. Critical point, C, was estimated by linear interpolation of the smallest eigenvalues of the tangential stiffness matrices $\mathbf{K}_{tA}$ and $\mathbf{K}_{tB}$. If $\gamma_A > 0$ is the smallest eigenvalue of $\boldsymbol{K}_{tA}$ and $\gamma_B < 0$ the smallest eigenvalue of $\boldsymbol{K}_{tB}$ the interpolation parameter α:

$$\alpha = \gamma_A / (\gamma_A - \gamma_B) \qquad \ldots (9)$$

takes the value between 0 and 1. The displacement vector at C, $\boldsymbol{u}_C$ and the corresponding load parameter λ_C were therefore approximated as:

$$\begin{aligned} \boldsymbol{u}_C &= \boldsymbol{u}_A + \alpha \Delta \boldsymbol{u}_{B-A} \\ \lambda_C &= \lambda_A + \alpha \Delta\lambda_{B-A} \end{aligned} \qquad \ldots (10)$$

where $\Delta\mathbf{u}_{B-A} = \mathbf{u}_B - \mathbf{u}_A$ and $\Delta\lambda_{B-A} = \lambda - \lambda_A$. It is worth noting that while eigenvalue extraction for large problems is computationally expensive, it may be shown[26] that λ and the corresponding eigenvector **φ**, may be extracted directly from the $\mathbf{LDL}^T$ decomposition of $\mathbf{K}_t$:

$$\lambda \approx \frac{(d_{ii})_{min}}{|\boldsymbol{l}_i|^2} \qquad \boldsymbol{\varphi} \approx \frac{\boldsymbol{l}_i}{|\boldsymbol{l}_i|} \qquad \ldots (11)$$

where $(d_{ii})_{min}$ is the smallest diagonal entry in **D** and $\mathbf{l}_i$ is the corresponding column of $(L^T)^{-1}$.

The critical eigenvector **φ** , at point C, may be determined from the tangential stiffness $\mathbf{K}_{tC}$. At this point the nature of this critical point may be determined by noting the following conditions:

$$\begin{aligned} \boldsymbol{\varphi}^T \boldsymbol{f}_{ext} \neq 0 \quad &\Rightarrow \quad \textit{limit point} \\ \boldsymbol{\varphi}^T \boldsymbol{f}_{ext} \approx 0 \quad &\Rightarrow \quad \textit{bifurcation point} \end{aligned} \qquad \ldots (12)$$

As has already been discussed, using a standard Newton-Raphson scheme would fail to converge. If imperfections were added to the panel geometry then it is likely that a limit point is encountered but this would depend on the nature of this imperfection. Provided that the arc-length method was implemented for the quasi-static response, there is a high probability of the solution being able of traversing this point. Even so, if the limit point is very sharp this may still lead to convergence difficulties. For this present study, the checks in Equation (12) were not carried out and the solution was switched to the pseudo-transient scheme when a critical point was encountered.

The choice of suitable starting parameters for the pseudo-transient phase is important to ensure that the solution does not 'back-track' along the same equilibrium path. Use is made of the orthogonality of the eigenvector, **φ**, with respect to the deformation state at the critical point. Point D in Fig. 11(b) denotes the starting conditions for the pseudo-transient phase. Point C_1 may be considered as a point above the critical point C without eigenmode injection. Equation (13) gives the initial conditions for the pseudo-transient phase:

$$\begin{aligned} \boldsymbol{u}_D &= \boldsymbol{u}_A + \alpha \Delta \boldsymbol{u}_{B-A} + \mu \boldsymbol{\varphi} \\ \lambda_D &= \lambda_A + \tilde{\alpha} \Delta\lambda_{B-A} \qquad \text{where } \tilde{\alpha} = \alpha + \delta\alpha \end{aligned} \qquad \ldots (13)$$

and μ and δα are parameters that define a small perturbation. The transient phase is stepped through pseudo-time until a steady-state response is reached upon which the solution scheme switches back to the quasi-static method.

4.0 NUMERICAL ANALYSIS

4.1 I-stiffened panel

The I-stiffened panel, I-P1, discussed in Section 2.1, was modelled using an in-house finite element code FE77XM[27] which incorporated the developments presented in Section 3.3. The panel model was developed using quadratic three-dimensional thick-shell composite elements incorporated in the code[28]. This allowed for detailed modelling of the stiffeners' geometric features including the flange taper (refer to Fig. 2) and the curvatures of the transition sections between the flanges and the stiffener webs as shown in Fig. 12. This element, like a brick element, has only translational degrees of freedom although, like a plate, the strains are defined in the local directions of the mid-surface plane.

Each skin bay was modelled using 46 elements along the length and eight elements along the width. The triangular regions at the foot and top of the web were filled with resin and therefore these regions were modelled using material properties corresponding to the composite resin 914C. No initial imperfections were introduced into the panel to remove bifurcations points since the solution procedure switched to the transient scheme whenever the tangential stiffness matrix was no longer positive definite indicating the presence of a critical point. Figure 13 shows the location of back-to-back strain gauges and LVDT which were used to validate the numerical model.

Skin buckling into five half-waves occurred at a loading of 110kN which compared favourably with the experimental value of 120kN. Figure 14(a) shows a comparison of a contour plot of out-of-plane displacements with the Moiré fringe pattern, obtained from experiment, just beyond initial buckling. Figure 14(b) shows the gradual development of the five half-wave patterns in the three-skin-bays. Between 250kN and 254kN the model underwent a mode-jump to six half-waves in all skin-bays, consistent with the behaviour observed experimentally and in good quantitative agreement with the finite element solution where this was observed to occur at 244kN (Fig. 14(c)).

Deep in the postbuckling regime the correlation was comparatively poor. The finite element model predicted a jump at a loading of 553kN, associated with the change in buckled pattern at the outer edges of the panel. This was 13·8% higher than the load at which a mode-jump was observed experimentally, characterised by the outer skin-bays jumping to seven half-waves while the central skin-bay remained at six-half waves until failure. The buckled patterns on the outer skin-bays of the finite element model were observed to undergo a gradual change following the change in deformation of the outer edges. As shown in Fig. 14(d), the second half-waves from the bottom edge of the panel are shown to elongate and exhibit an 'hourglass' contour pattern which has been shown to be a precursor to a mode-jump[4]. It is therefore postulated that in the experiment, mode-jumps in the outer edges may have triggered the jump in the outer skin-bays while computationally, this influence seemed to have happened gradually where the outer skin-bays did eventually

https://doi.org/10.1017/S0001924000004899 Published online by Cambridge University Press

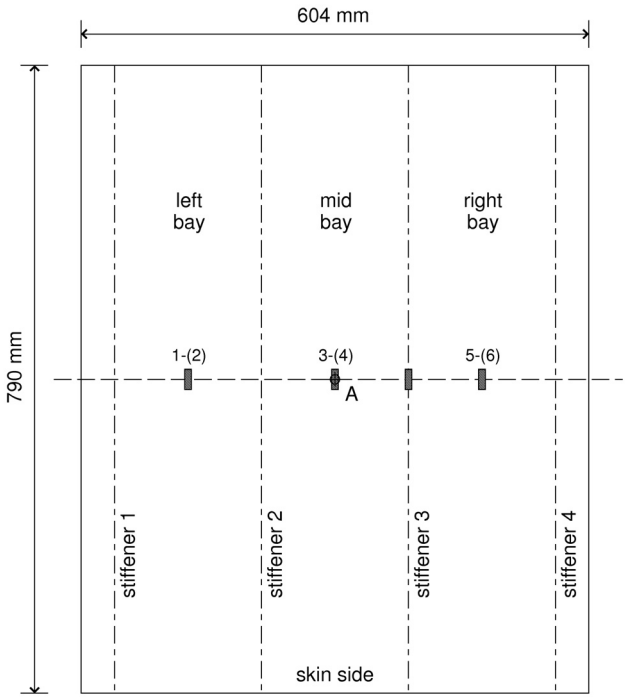


Figure 13. I-stiffened panel, I-P2, showing back-to-back strain-gauges and LVDT location (a bracketed strain-gauge number denotes a strain gauge mounted on the stiffener side).

undergo a mode-jump but at a loading of 647kN. This discrepancy was due to the considerable extent of matrix micro-cracking which occurred under this high compressive loading, reducing the overall stiffness and leading to the observed secondary mode-jump occurring earlier than predicted. This damage was not accounted for in the finite element model. Figure 15 shows the out-of-plane displacement measured by the LVDT. Figures 16-18 show the results of back-to-back strain gauges at locations shown in Fig. 13. It is seen that good correlation is achieved for most of the loading history before the effects of matrix cracking become significant.

4.2 Hat-stiffened panel

A finite element analysis of this panel was undertaken, using a similar approach to that adopted for the I-stiffened panel described in the previous section. Fig. 19(a) and Fig. 19(b) show the Moiré fringe patterns before and just after structural failure, respectively. This failure was characterised by stiffener debonding at a loading of 380kN. Contour plots, obtained form the finite element analysis, are shown in Figs 19(c) and 19(d). A mode-jump associated with the sudden change in buckling deformation of the central skin-bay, from five half-waves (Fig. 19(c)) to seven half-waves (Fig. 19(d)) occurred at 385kN, Displacements and strains, obtained experimentally at various locations on the panel, were also compared with those extracted from the analysis. Fig. 20 shows the out-of-plane displacement measured at the centre of the panel, marked '*A*' on the inset diagram. What is significant is that the finite element analysis predicted a mode-jump at a loading of 385kN which is remarkably close to the load at which failure of the panel occurred. This close agreement is also evident from the back-to-back strain gauge results in Fig. 21, obtained at the location marked '*B*' on the inset diagram.

It should be noted that in the experiment, this mode-jump was associated with a change in mode-shape of the right skin-bay from

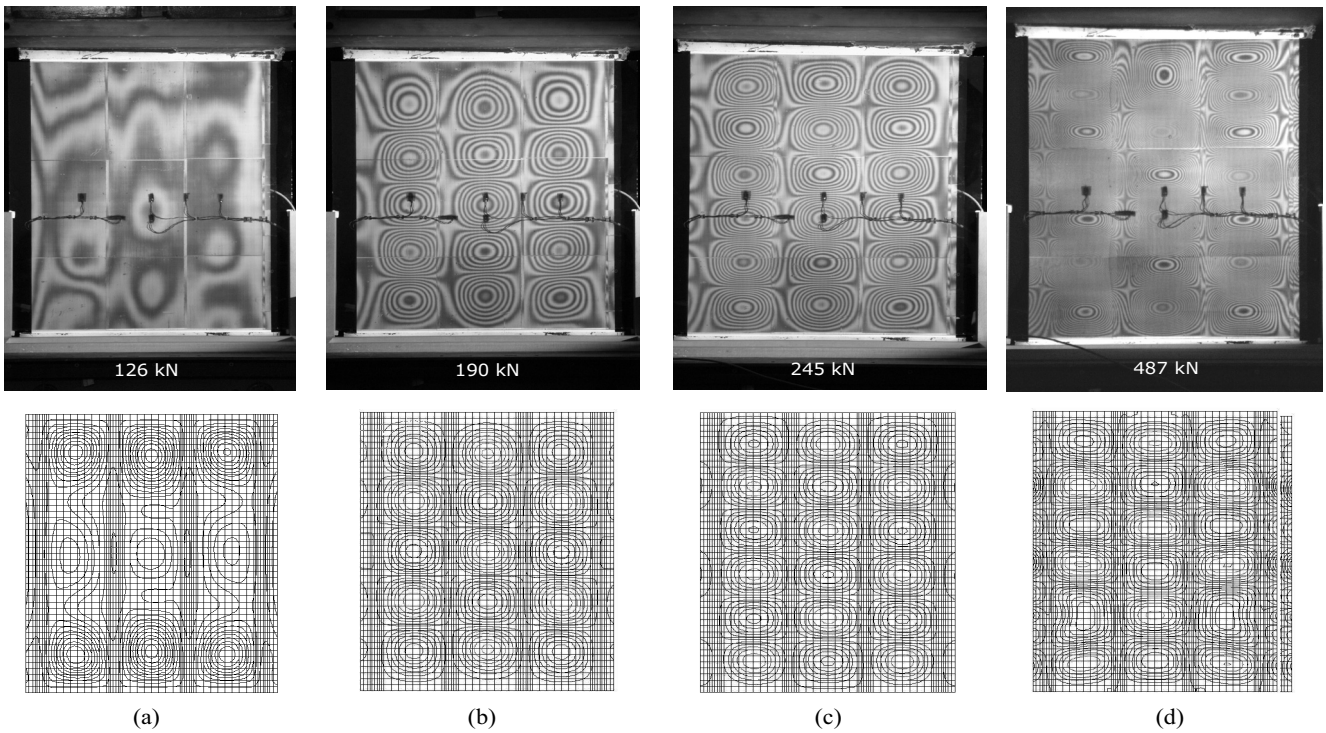


Figure 14. Shadow Moiré fringe patterns at different load levels (top) and corresponding finite element contour plots of out-of-plane displacements (bottom).

https://doi.org/10.1017/S0001924000004899 Published online by Cambridge University Press

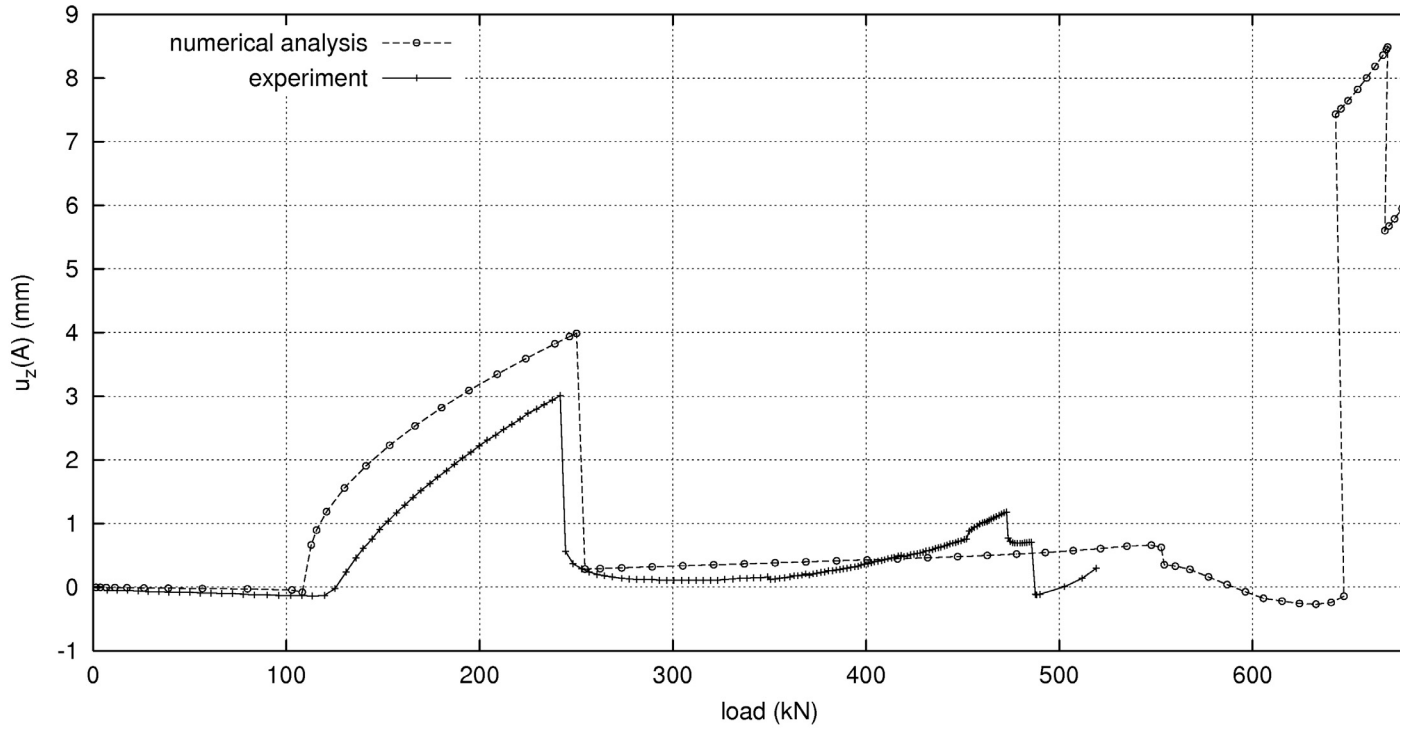


Figure 15. Out-of-plane displacement at the centre of panel I-P1 (point A in Fig. 13).

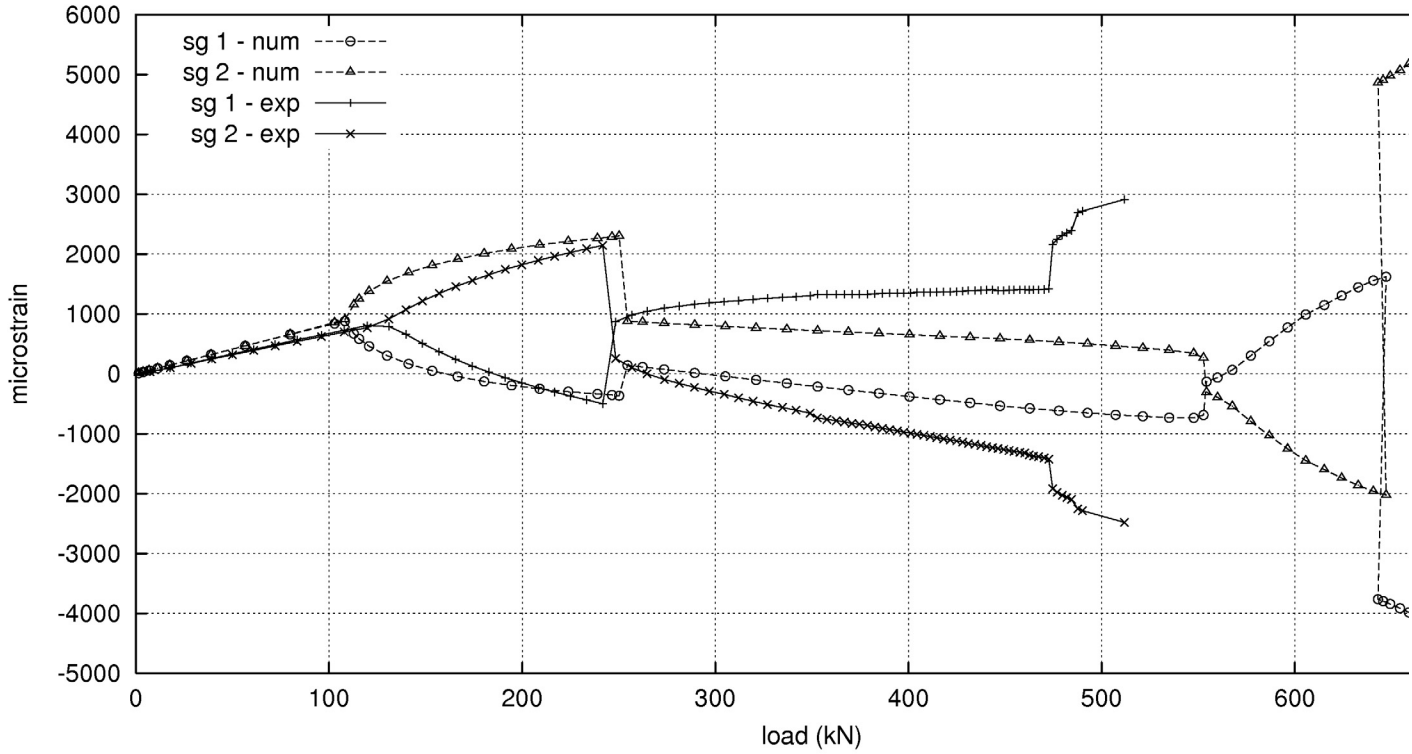


Figure 16. Back-to-back strain gauge pair 1-2 on panel I-P1 (location shown in Fig. 13).

five to six half-waves. With reference to Fig. 19(a), the lower half-wave of the central skin-bay is observed to be on the verge of splitting into two half-waves, a precursor to mode-jumping. It is therefore plausible that the initiation of a mode-jump in this skin-bay, and not the mode-jump in the right skin-bay, precipitated failure. The release of internal stresses and changes in the boundary conditions of this skin-bay, arising from skin-stiffener debonding, meant that a new higher mode-shape could not be sustained. The finite element analysis underwent an initial mode-jump at a loading of 198kN where the outer skin-bay changed from five to six half-

https://doi.org/10.1017/S0001924000004899 Published online by Cambridge University Press

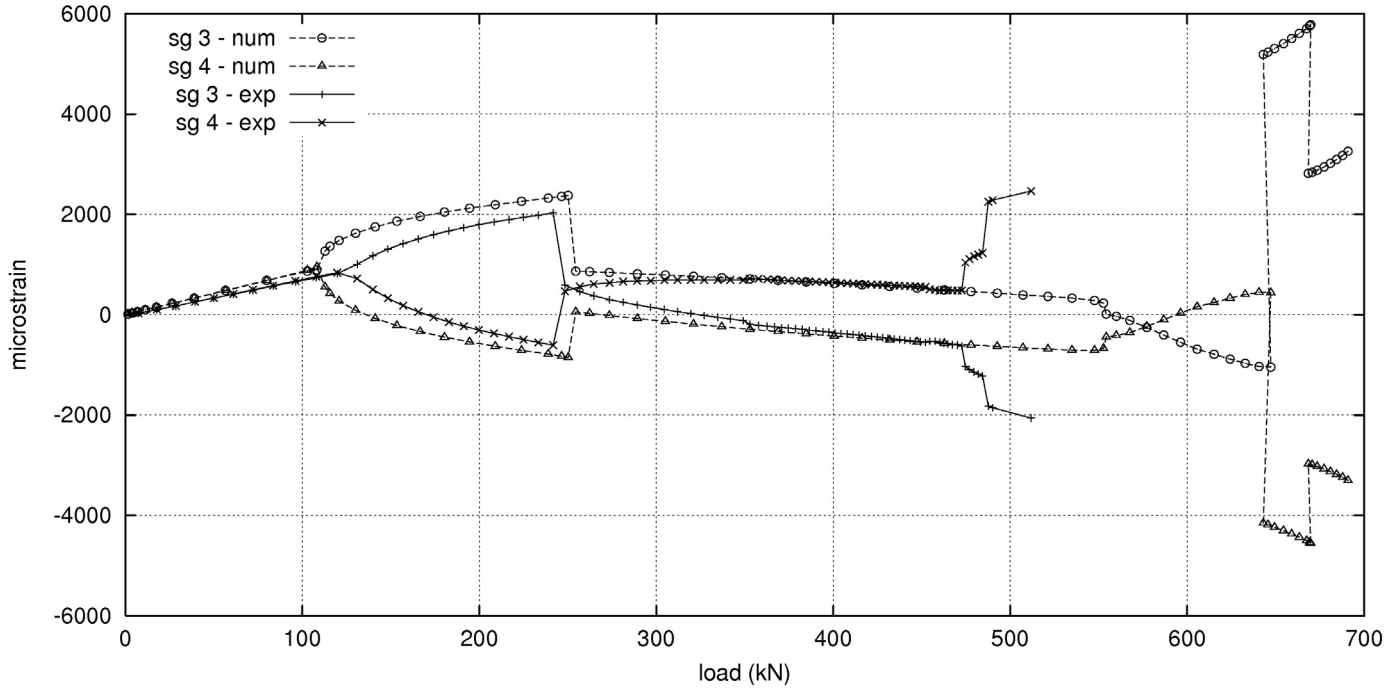


Figure 17. Back-to-back strain gauge pair 3-4 on panel I-P1 (location shown in Fig. 13).

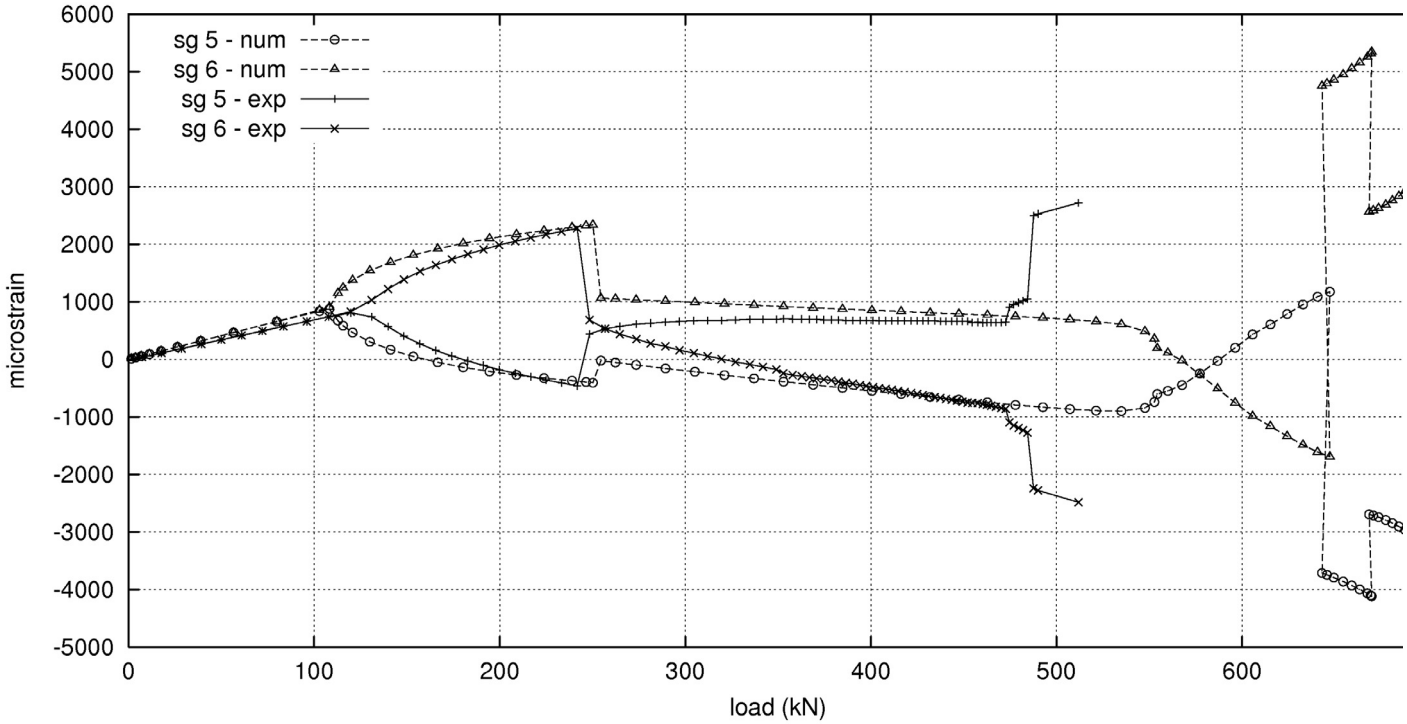


Figure 18. Back-to-back strain gauge pair 5-6 on panel I-P1 (location shown in Fig. 13).

waves. The mode-jump at 385K was associated with the central skin-bay changing from five to seven half-waves.

This study supports earlier indirect observations which hinted at the possibility of structural failure occurring at a mode-jump. It is through the development of an accurate and robust numerical finite element solution scheme that this trigger to structural failure is given credence. Further investigations into the secondary bonding of this panel revealed that there were regions at the interface where the bonding was defective (Araldite 2015 was used to bond the stiffeners to the skin). It is suggested that the short-duration high displacements and strains, which were shown to occur during the testing of the I-P2 panel using the high-speed DSP system and presented in Section 2.1, initiated failure in this panel.

https://doi.org/10.1017/S0001924000004899 Published online by Cambridge University Press

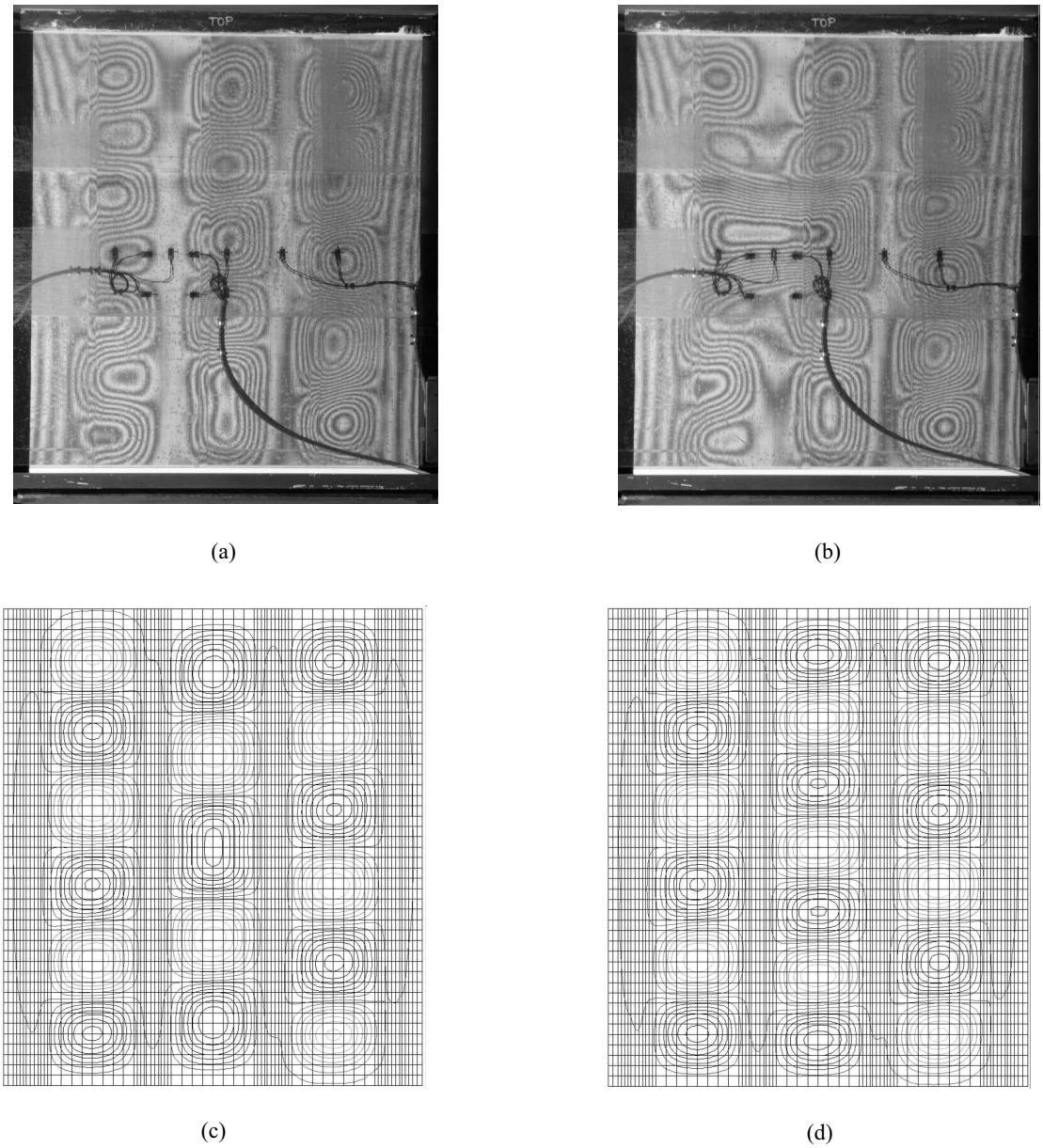


Figure 19. (a) Moiré fringe pattern of hat-stiffened panel at a loading just before failure at 380kN (b) Moiré fringe pattern at failure (c) Finite element contour plot just before mode-jump at 385kN (d) Finite element contour plot just after mode-jump.

5.0 CONCLUSIONS

The phenomenon of mode-jumping was investigated using high speed digital speckle photogrammetry. The mode-jump event, recorded for an I-stiffened panel, was shown to last approximately 106 milliseconds. The out-of-plane displacement and in-plane longitudinal strain responses were characterised by high-frequency oscillations with peaks which were considerably higher than the static values obtained just after the mode-jump when the transient behaviour had subsided. Strain/stress reversal was not observed in any region of the panel during this transient phase.

It was postulated, and subsequently shown, that mode-jumping may release enough energy to cause failure, particularly in vulnerable regions within a structure. A robust strategy was presented to reliably capture this behaviour where the solution scheme automatically switched from a standard non-linear quasi-static algorithm to a more robust pseudo-transient one when a critical point along an equilibrium path was encountered.

The experimental results of an I-stiffened and a hat-stiffened panel were compared with the results predicted by the finite element model and good agreement was achieved in predicting the mode-jump. The hat-stiffened panel was shown to have failed at a load corresponding to a mode-jump and confirmed earlier indirect evidence of this type of structural failure. Deep into the postbuckling regime, the inevitable matrix-cracking in the tested I-stiffened panel, not accounted for in the composite material's behaviour in the finite element model, resulted in poorer correlation between the experimental and numerical results. Further work is currently underway to include in-plane and out-of-plane damage models to enable a more accurate representation of the structural response of composite panels under failure-inducing loads

https://doi.org/10.1017/S0001924000004899 Published online by Cambridge University Press

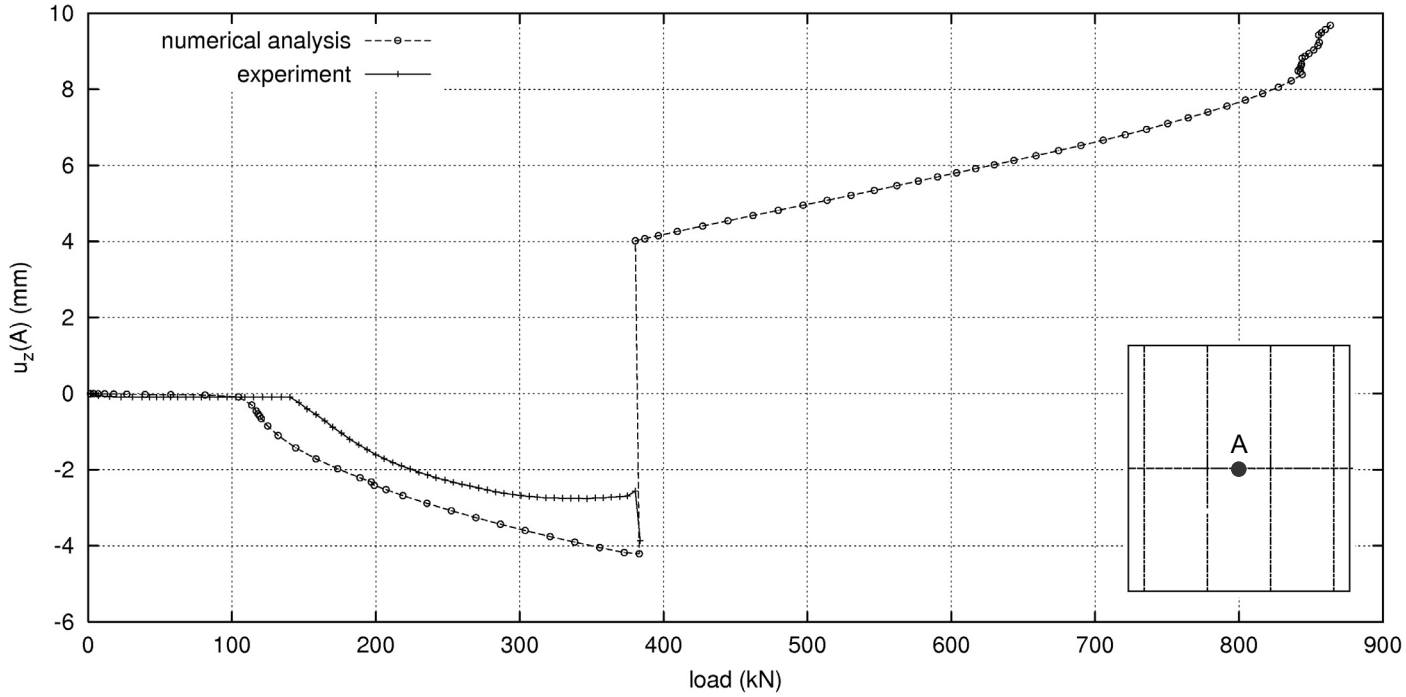


Figure 20. Out-of-plane displacement at centre of hat-stiffened panel marked by point A.

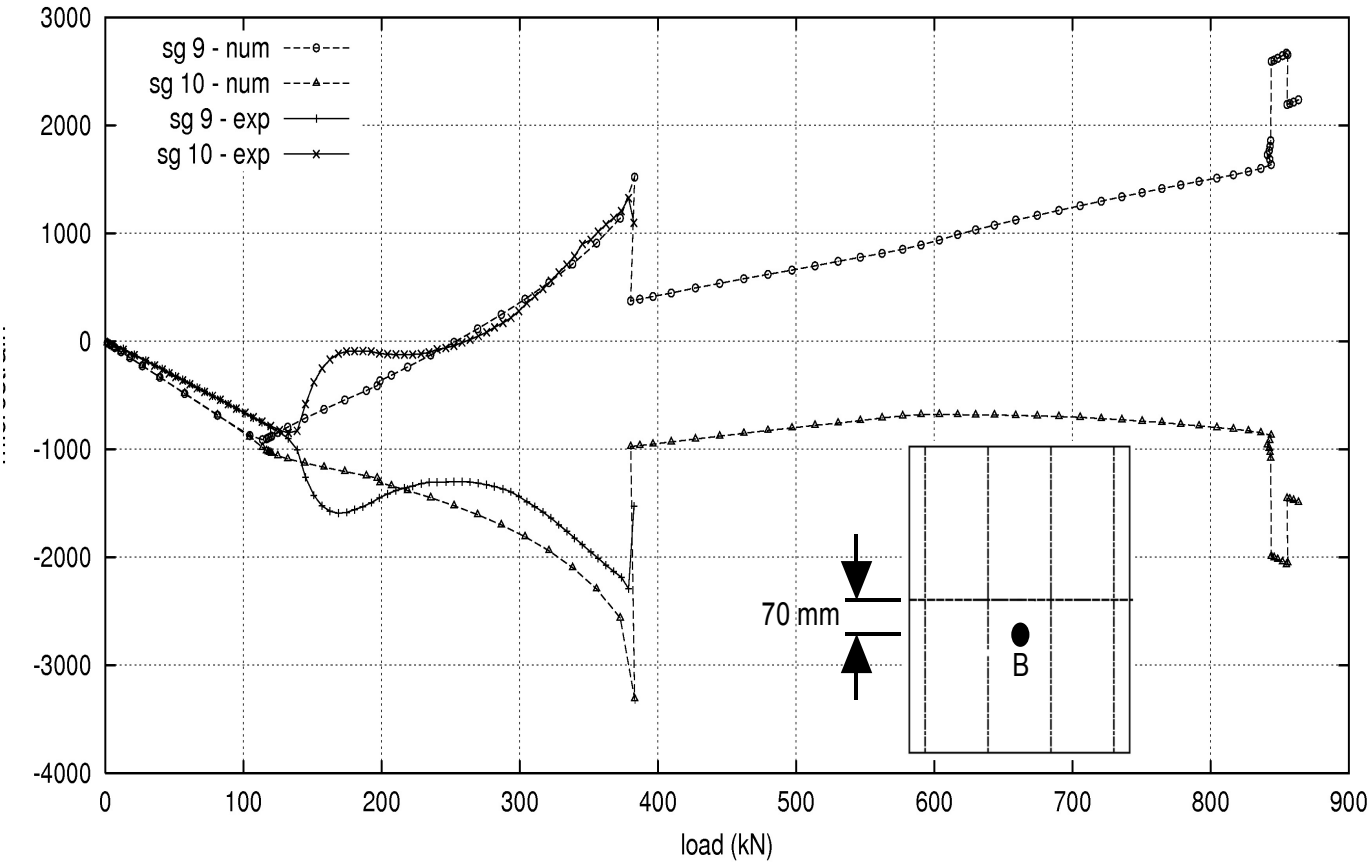


Figure 21. Back-to-back strain gauges 9/10 on hat-stiffened panel marked by point B (gauge 10 is on stiffener side).

https://doi.org/10.1017/S0001924000004899 Published online by Cambridge University Press

ACKNOWLEDGEMENT

The main body of work presented in this paper was funded by the Engineering and Physical Sciences Research Council (EPSRC) under contract no GR/R32147/01. The use of the high-speed digital speckle photogrammetry at DLR, Braunschweig, was made possible through the award of a European Union grant under the 'Access to Research Infrastructures' scheme. A special thanks to Mr Hans Christian Goetting and Mr Ary Zipfel at DLR's Institute of Structural Mechanics for their considerable expertise in planning the test programme and for their assistance in post-processing the data.

REFERENCES

1. FALZON, B.G. and STEVEN, G.P. Buckling mode transition in hat-stiffened composite panels loaded in uniaxial compression, *Compos Struct*, 1997, **37**, (2), pp 253-267.
2. FALZON, B.G., STEVENS, K.A. and DAVIES, G.A.O. Postbuckling behaviour of a blade-stiffened composite panel loaded in uniaxial compression, *Compos Part A: Appl Sci Manuf*, 2000, **31**, (5), pp 459-468.
3. STEVENS, K.A., RICCI, R. and DAVIES, G.A.O. Buckling and postbuckling of composite structures, *Composites*, 2001, **26**, (3), pp 189-199.
4. FALZON, B.G. The behaviour of damage tolerant hat-stiffened composite panels loaded in uniaxial compression, *Compos Part A: Appl.Sci Manuf*, 2001, **32**, (9), pp 1255-1262.
5. FALZON, B.G. and HITCHINGS, D. Capturing mode-switching in postbuckling composite panels using a modified explicit procedure, *Compos Struct*, 2003, **60**, (4), pp 447-453.
6. FALZON, B.G. and CERINI, M. An automated hybrid procedure for capturing mode-jumping in postbuckling composite stiffened structures, *Compos Struct*, 2006, **73**, (2), pp 186-195.
7. STARNES, J.H., KNIGHT, N.F. and ROUSE, M. Postbuckling behaviour of selected flat stiffened graphite-epoxy panels loaded in compression, *AIAA J*, 1985, **23**, (8), pp 1236-1246.
8. ROMEO, G. Experimental investigation on advanced composite stiffened structures under uniaxial compression and bending, *AIAA J*, 1986, **24**, (11), pp 1823-1830.
9. LANZI, L. A numerical and experimental investigation on composite stiffened panels into post-buckling, *Thin Wall Struct*, 2004, **42**, pp 1645-1664.
10. CAPUTO, F., ESPOSITO, R., PERUGINI, P. and SANTORO, D. Numerical-experimental investigation on post-buckled stiffened composite panels, *Compos Struct*, 2002, **55**, (3), pp 347-357.
11. Group of Personalities, *European Aeronautics: A Vision for 2020*, 2001, Office for Official Publications of the European Communities, Belgium.
12. ROMEO G. and FRULLA, G. Non-linear analysis of anisotropic plates with initial imperfections and various boundary conditions subjected to combined biaxial compression and shear loads, *Int J Solids Struct*, 1994, **31**, (6), pp 763-783.
13. WEMPNER, G.A. Discrete approximations related to nonlinear theories of solids, *Int J Solids Struct*, 1971, **7**, 1581-1599.
14. RIKS, E. An incremental approach to the solution of snapping and buckling problems, *Int J Solids Struct*, 1979, **15**, pp 529-551.
15. CRISFIELD, M.A. A fast incremental/iterative solution procedure that handles 'snap-through', *Comput Struct*, 1981, **13**, pp 55-62.
16. RIKS, E., RANKIN, C.C. and BROGAN, F.A. On the solution of mode-jumping phenomena in thin-walled shell structures, *Comput Meth Appl M*, 1996, **136**, (1), pp 59-92.
17. SINGER, J., ARBOCZ, J. and WELLER, T. B*uckling Experiments: Experimental Methods in Buckling of Thin Walled Structures*, 1998, Vol 1, John Wiley & Sons, Chichester, UK.
18. BUSHNELL, C., RANKIN, C. and RIKS, E. Optimization of stiffened panels in which mode-jumping is accounted for, 1998, in *Stability Analysis of Plates and Shells: A Collection of Papers in Honor of Dr. Manuel Stein*, NASA/CP-1998-206280, pp 105-145.
19. ARAMIS: Deformation measurement using the grating method, 200, GOM, Braunschweig, Germany.
20. CERINI, M. Investigation of Secondary Instabilities in Postbuckling Stiffened Composite Structures, 2005, PhD thesis, Imperial College London, UK.
21. FALZON, B.G. and HITCHINGS, D. *An Introduction to Modelling Buckling and Collapse,* 2006, NAFEMS, Glasgow, UK.
22. BATOZ, J.L. and DHATT, G. Incremental displacement algorithms for non-linear problems, *Int J Numer Meth Eng*, 1979, **14**, pp 1262-1266.
23. CRISFIELD, M.A. *Non-linear Finite Element Analysis of Solids and Structures,* 1991: Vol 1, John Wiley & Sons Ltd, Chichester, UK.
24. BISAGNI, C. Numerical analysis and experimental correlation of composite shell buckling and post-buckling, *Compos Part B-Eng*, 2000, **31**, (8), pp 655-667.
25. CRISFIELD, M.A. *Non-linear Finite Element Analysis of Solids and Structures,* 1997, Vol 2, John Wiley & Sons Ltd, Chichester, UK.
26. FUJII, F., AND NOGUCHI, H., The buckling mode extracted from the LDLT-decomposed larger-order stiffness matrix, *Commun Numer Meth En*, 2002, **18**, (7), pp 459-467.
27. CERINI, M., FALZON, B.G. and HITCHINGS, *D. FE77XM User Manual*, 2005, Imperial College London.
28. FALZON, B.G., HITCHINGS, D. and BESANT, T. Fracture mechanics using a 3D composite element, *Compos Struct*, 1999, **45, (1**), pp 29-39.

https://doi.org/10.1017/S0001924000004899 Published online by Cambridge University Press